Self-consistent embedding quantum mechanics/molecular mechanics method with applications to metals

Xu Zhang, Qing Peng, and Gang Lu
Department of Physics and Astronomy, California State University Northridge, Northridge, California 91330-8268, USA
(Received 9 June 2010; published 21 October 2010)

We present a quantum mechanics (QM)/molecular mechanics (MM) method for coupling Kohn-Sham density-functional theory with classical atomistic simulations based on a self-consistent embedding theory. The formalism and numerical implementation of the method are described. The QM/MM method is employed to study extended defects—a grain boundary and an edge dislocation in Al by focusing on hydrogen (H)-defect interactions. We find that it is energetically more favorable for H impurities to segregate at the grain boundary and the dislocation core as opposed to the bulk. We provide direct first-principles evidence that both the grain boundary and the dislocation could serve as a "pipe" to accelerate H diffusion and shed light on the corresponding atomistic mechanisms. The results demonstrate that the QM/MM method is a powerful approach in dealing with extended defects in materials.

DOI: 10.1103/PhysRevB.82.134120 PACS number(s): 61.72.Lk, 71.15.Mb, 71.15.Dx

I. INTRODUCTION

Despite the ever increasing computational power, modeling, and simulation of complex material problems at atomic level still remain a challenge.[1] For example, quantum mechanics (QM) is mandatory for a proper treatment of bond breaking, charge transfer, electron excitation, magnetism, etc., in materials. However, owing to its computational demand, the application of QM has been limited to relatively small systems consisting of up to a few hundred atoms. On the other hand, atomistic simulations based on empirical interatomic potentials are often capable of describing small-amplitude vibrations and torsions, elastic deformation and electrostatic interactions, etc., in many material systems. Termed as molecular mechanical (MM) methods, these empirical atomistic approaches can deal with millions of atoms or even more. Therefore algorithms that combine quantum mechanics and molecular mechanics (QM/MM) poise to offer a promising solution to the computational challenge in materials science.[1–3] Unfortunately, in contrast to a vast and growing number of QM/MM applications in chemistry and biochemistry,[3–5] much fewer QM/MM simulations have been attempted in materials science, and particularly for metals.

Based on how the interaction energy between QM and MM is formulated, QM/MM methods can be divided into two categories: mechanical coupling and quantum coupling. With the mechanical coupling, the interaction energy is calculated at the MM level whereas the interaction energy is calculated at the QM level with the quantum coupling.[3] For many molecular systems that are of interest in chemistry and biochemistry, one can partition the system into QM and MM parts by cutting the chemical bonds linking the two parts and then saturate the dangling bonds at the boundary of QM region by so-called link atoms.[3,5] This procedure and the similar ones can be justified because of the presence of well defined and localized chemical bonds in such molecular systems. The mechanical coupling methods that are based on the cutting/saturating chemical bonds have seen wide applications in chemistry and biochemistry.[3–5] On the other hand, for metallic materials, the procedure is not longer valid owing to the delocalized nature of metallic bonding; it becomes impractical to cut and saturate bonds. In fact the very concept of bond becomes less appropriate than the band picture for metals. Therefore, more sophisticated ideas have to be developed to deal with metallic cohesion and bands represented by the delocalized electron states across the QM/MM boundary. One of such ideas is the self-consistent embedding theory[6–13] which is based on the quantum coupling. The embedding theory provides a general and potentially rigorous framework for QM/MM coupling. The theory can be applied to both metallic and covalently bonded systems and does not depend on the spatial locality and the link atoms that are indispensable in other coupling methods. For example, Hodak *et al.*[13] have developed a QM/MM embedding method to study biological systems with covalent bonds. In this paper, we are interested in the QM/MM method which is suitable for metallic systems.

Since the most natural basis to expand the electron wave functions in metals is plane waves, we will focus on a plane wave, pseudopotential implementation of the self-consistent embedding theory. The mathematical simplicity and computational efficiency associated with the plane-wave basis—such as the possibility of working in reciprocal space and of using the fast Fourier transform (FFT), have rendered the method particularly attractive. Moreover, we have implemented the method in the popular Vienna *ab initio* simulation package (VASP),[14–16] taking full advantage of the numerical and computational prowess of VASP. Finally since the method can provide both energy and force, it can be used easily in molecular dynamics, energy barrier calculations in conjunction with nudged elastic band method (NEB) (Ref. 17) and many other features that have been included in VASP.

In our previous QM/MM work, we have introduced a QM/MM method that employs orbital-free density-functional theory (OF-DFT) (Refs. 18–20) for treating the QM region.[10] However, for many material problems, the existing OFDFT functionals may not be sufficiently accurate for the QM region. Therefore it is desirable to develop an embedding QM/MM method with the Kohn-Sham DFT (KS-DFT) for treating the QM region.

Hydrogen (H) is a major reactant with solids as a result of its high mobility and strong chemical reactivity. An understanding of the interactions between H and extended defects is of considerable importance to kinetic, mechanical, and thermodynamical properties of the materials.[21] In fact, these interactions are the ultimate culprit of H embrittlement of metals. In addition, recent interests in H storage materials and fuel cells create a sense of urgency in unraveling the complicated H-defect interactions at a fundamental level. In this paper, we examine H-dislocation and H-grain boundary (GB) interactions by focusing on H-defect binding, H site preference and H diffusion in the defects. The QM/MM method is ideal for treating H-defect interactions because it can capture both the short-range quantum mechanical interactions (including charge transfer, bond breaking, and formation, etc) at the defect core and the long-range elastic field of the extended defects. Furthermore, because it is extremely difficult in tracking atomic motion experimentally, very few direct measurements of H diffusion along grain boundaries or dislocations have been reported. Therefore theoretical investigations based on first principles are invaluable to provide accurate determination of H diffusion barriers and atomistic mechanisms in the extended defects.[22]

We first set up the stage with a brief introduction to the QM/MM embedding formalism by defining the key concepts and physical quantities. In Sec. II, we discuss two technical issues including the spin-polarization calculations and the construction of the Hamiltonian in reciprocal space. We also examine the physical behavior of the embedding potential which is central to the QM/MM embedding theory. In Sec. III we apply the QM/MM method to study the interactions between H impurities and the extended defects in Al. These examples are chosen to both validate and demonstrate the applicability of the method. Finally we conclude in Sec. IV with a brief discussion of future directions.

II. METHODOLOGY

A. Formalism

In general, the entire QM/MM system is partitioned into two regions: region I treated with QM and region II treated with MM, as shown in Fig. 1. Normally the region I is embedded into a much larger region II. Although different levels of QM simulations could be employed in the region I, we focus on the KS-DFT as mentioned in the introduction. Similarly while many empirical potentials could be used in the region II, we choose the embedded-atom method (EAM) (Ref. 23) as an example of MM calculations in the paper.

The total energy of the QM/MM system includes the energy of the region I, the energy for the region II, and the interaction energy between them. The self-consistent determination of the interaction energy at a quantum mechanical level is the hallmark of the present method. In specific, the total energy can be expressed as

$$E_{\mathrm{tot}}[\rho^{\mathrm{tot}};\mathbf{R}^{\mathrm{tot}}] = \min_{\rho^{\mathrm{I}}}\{E_{\mathrm{KS}}[\rho^{\mathrm{I}};\mathbf{R}^{\mathrm{I}}] + E_{\mathrm{OF}}^{\mathrm{int}}[\rho^{\mathrm{I}},\rho^{\mathrm{II}};\mathbf{R}^{\mathrm{I}},\mathbf{R}^{\mathrm{II}}]\} + E_{\mathrm{MM}}[\mathbf{R}^{\mathrm{II}}], \quad (1)$$

where $\mathbf{R}^{\mathrm{tot}} \equiv \mathbf{R}^{\mathrm{I}} \cup \mathbf{R}^{\mathrm{II}}$, $\mathbf{R}^{\mathrm{I}}$, and $\mathbf{R}^{\mathrm{II}}$ denote atomic coordinates

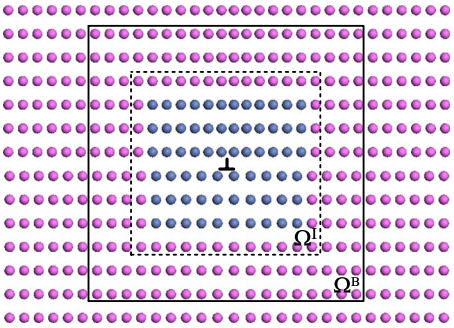

FIG. 1. (Color online) The schematic domain partition in the QM/MM method with an edge dislocation in Al as an example. The blue and magenta spheres represent region I and II atoms, respectively. The dashed box represents Ω^{I} and the solid box represents the periodic box Ω^{B}. The charge density of region I ρ^{I} is confined within Ω^{I}, and the periodic boundary conditions are imposed over Ω^{B}.

in the region I and II, respectively. The charge density of the region I, ρ^{I}, which is the degree of the freedom of the problem, is determined self-consistently by minimizing the total energy functional Eq. (1). We associate each MM atom in the region II with an atomic-centered electron density (ρ^{at}) and a pseudopotential; both of them are constructed *a priori*[10] and remain fixed during the QM/MM simulation. The charge density of the region II, ρ^{II}, is defined as a superposition of atomic-centered charge densities ρ^{at} via $\rho^{\mathrm{II}}(\mathbf{r}) = \Sigma_{i\in\mathrm{II}}\rho^{\mathrm{at}}(\mathbf{r}-\mathbf{R}_i)$, which only changes upon the relaxation of the region II ions. The total charge density ρ^{tot} is given by $\rho^{\mathrm{tot}} = \rho^{\mathrm{I}} + \rho^{\mathrm{II}}$. The interaction energy between the region I and II, $E_{\mathrm{OF}}^{\mathrm{int}}$, formulated by OF-DFT is defined as follows:

$$E_{\mathrm{OF}}^{\mathrm{int}}[\rho^{\mathrm{I}},\rho^{\mathrm{II}};\mathbf{R}^{\mathrm{I}},\mathbf{R}^{\mathrm{II}}] = E_{\mathrm{OF}}[\rho^{\mathrm{tot}};\mathbf{R}^{\mathrm{tot}}] - E_{\mathrm{OF}}[\rho^{\mathrm{I}};\mathbf{R}^{\mathrm{I}}] - E_{\mathrm{OF}}[\rho^{\mathrm{II}};\mathbf{R}^{\mathrm{II}}]. \quad (2)$$

The unique feature of OF-DFT is that it allows a QM calculation of energetics by knowing *only* the electronic density. The accuracy of OF-DFT is in between KS-DFT and EAM, which is consistent to its usage in the QM/MM method. In other words, just as the errors of KS-DFT and EAM are in the region I and II, respectively, the errors of the OF-DFT coupling is localized at the interface of the region I and II. Finally, the EAM method was developed to treat metallic systems by approximating the density of the solid as a superposition of charge densities of isolated atoms. The success of EAM in capturing the energetics of metallic systems, combined with its DFT foundation, make it an ideal candidate in the present QM/MM method. $\mu_{\mathrm{emb}}[\rho^{\mathrm{I}},\rho^{\mathrm{II}}]$ termed as embedding potential, is of crucial importance to the QM/MM method, and is defined as a functional derivative of the interaction energy $E_{\mathrm{OF}}^{\mathrm{int}}$ with respect to ρ^{I},

$$\mu_{\mathrm{emb}}(\mathbf{r}) \equiv \frac{\delta E_{\mathrm{OF}}^{\mathrm{int}}[\rho^{\mathrm{I}},\rho^{\mathrm{II}};\mathbf{R}^{\mathrm{I}},\mathbf{R}^{\mathrm{II}}]}{\delta\rho^{\mathrm{I}}}. \quad (3)$$

$\mu_{\mathrm{emb}}(\mathbf{r})$ represents the effective single-particle potential that the region I electrons feel due to the presence of the region II atoms (both electrons and ions).

In this paper, the plane-wave pseudopotential method implemented in the VASP package is employed for the KS-DFT simulation of the region I. The minimization of the total QM/MM energy [Eq. (1)] with respect to ρ^{I} leads to a self-consistent solution of the KS-type eigenvalue equations. The QM/MM coupling is achieved by including the embedding potential in the generalized KS equation; both $\mu_{\mathrm{emb}}(\mathbf{r})$ and KS equations have to be solved self-consistently. The detailed expressions for the interaction energy and the embedding potential can be found in Refs. 10 and 11 and are not duplicated here.

The QM/MM method can also deal with collinear spin-polarized systems. Specifically, the charge density $\rho^{\mathrm{I}}(\rho^{\mathrm{II}})$ is assumed to have two components, one for spin up $\rho^{\mathrm{I}\uparrow}(\rho^{\mathrm{II}\uparrow})$ and the other for spin down $\rho^{\mathrm{I}\downarrow}(\rho^{\mathrm{II}\downarrow})$. Since $\rho^{\mathrm{II}\uparrow}(\rho^{\mathrm{II}\downarrow})$ is the superposition of $\rho^{\mathrm{at}\uparrow}(\rho^{\mathrm{at}\downarrow})$, $\rho^{\mathrm{at}\uparrow}$, and $\rho^{\mathrm{at}\downarrow}$ have to be constructed *a priori*. In this way, $E_{\mathrm{xc}}^{\mathrm{int}}$ and $\mu_{\mathrm{xc}}^{\mathrm{emb}\uparrow(\downarrow)}$ can be calculated by

$$E_{\mathrm{xc}}^{\mathrm{int}} = E_{\mathrm{xc}}[\rho^{\mathrm{tot}\uparrow},\rho^{\mathrm{tot}\downarrow}] - E_{\mathrm{xc}}[\rho^{\mathrm{I}\uparrow},\rho^{\mathrm{I}\downarrow}] - E_{\mathrm{xc}}[\rho^{\mathrm{II}\uparrow},\rho^{\mathrm{II}\downarrow}],$$

$$\mu_{\mathrm{xc}}^{\mathrm{emb}\uparrow} = \mu_{\mathrm{xc}}^{\uparrow}[\rho^{\mathrm{tot}\uparrow},\rho^{\mathrm{tot}\downarrow}] - \mu_{\mathrm{xc}}^{\uparrow}[\rho^{\mathrm{I}\uparrow},\rho^{\mathrm{I}\downarrow}],$$

$$\mu_{\mathrm{xc}}^{\mathrm{emb}\downarrow} = \mu_{\mathrm{xc}}^{\downarrow}[\rho^{\mathrm{tot}\uparrow},\rho^{\mathrm{tot}\downarrow}] - \mu_{\mathrm{xc}}^{\downarrow}[\rho^{\mathrm{I}\uparrow},\rho^{\mathrm{I}\downarrow}], \quad (4)$$

where $\mu_{\mathrm{xc}}^{\mathrm{emb}\uparrow}$ and $\mu_{\mathrm{xc}}^{\mathrm{emb}\downarrow}$ act upon $\rho^{\mathrm{I}\uparrow}$ and $\rho^{\mathrm{I}\downarrow}$, respectively.

B. Construction of Hamiltonian in reciprocal space

In the plane-wave basis, the Hamiltonian $\mathbf{H}(\mathbf{k})$ is constructed in the reciprocal space as a function of $\mathbf{k}$, where $\mathbf{k}$ is in the first Brillouin zone. In this Hamiltonian, the Hartree potential $V_{\mathrm{H}}(\mathbf{G})$ and the local pseudopotential $V_{\mathrm{loc}}^{\mathrm{ion}}(\mathbf{G})$ are calculated in the reciprocal space directly.[24] G is the reciprocal lattice vector. On the other hand, the exchange-correlation potential V_{xc} and the embedding potential μ_{emb} are evaluated in the real space first, and are then transformed to the reciprocal space by the FFTs. Once the Hamiltonian is constructed, it is solved in the reciprocal space so that the ground state KS orbitals, the KS eigenvalues, the electron density and eventually the total energy can be determined accordingly. Since $\mu_{\mathrm{emb}}(\mathbf{r})$ depends on $\rho^{\mathrm{I}}(\mathbf{r})$ and $\rho^{\mathrm{II}}(\mathbf{r})$, for a given ionic configuration, $\rho^{\mathrm{II}}(\mathbf{r})$ has to be constructed *a priori* and remains fixed during the minimization of Eq. (1).

In the KS-DFT plane-wave calculation of the region I, we introduce a box Ω^{B} as shown in Fig. 1 over which the periodic boundary conditions (PBC) are imposed. The PBC are necessary for various FFTs which are crucial for efficient numerical calculations. In the following, we justify the use of the PBC with the realization that the real QM/MM system is nonperiodic. The justification is analogous to the one employed in the periodic slab calculations of surfaces. In the slab model, the wave functions and the electron density of the surface are assumed to decay exponentially so that they are vanishing at the end of the slab vacuum, introduced at some distance away from the surface. Therefore, the PBC do not lead to appreciable errors since there is no overlap of the wave functions and the electronic density from the neighboring cells. In the QM/MM case, the basic ansatz is that ρ^{I} is confined within Ω^{I} so that the wave functions and the charge density of the region I decay to zero beyond Ω^{I}. Thus as long as the vacuum introduced between Ω^{I} and Ω^{B} is large enough, it can effectively eliminate the fictitious interaction between the periodic images.

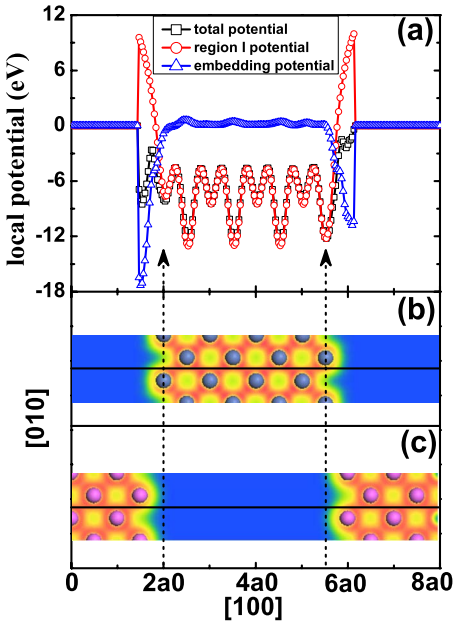

FIG. 2. (Color online) (a) Total local potential, local potential in the region I, and the embedding potential are plotted along a straight line in [100] direction for a perfect Al lattice. The position of the straight horizontal line is indicated in (b) and (c). Charge density ρ^{I} and ρ^{II} in x-y plane are plotted in (b) and (c), respectively. The blue (magenta) spheres represent the region I (II) ions, and the contour scale (in $\mathrm{Å}^{-3}$) ranges from 0.0 (blue) to 0.225 (red).

C. Embedding potential

The embedding potential represents the physical effect that the electrons in the region I feel due to the presence of the region II. Without the embedding potential, ρ^{I} will correspond to the charge density of a bare cluster. The presence of the embedding potential is thus to remove the fictitious surface states and render a realistic description of ρ^{I}.[11]

Here, we take Al as an example to examine the behavior of the embedding potential. We choose a perfect lattice of Al containing $14a_0 \times 14a_0 \times a_0$ (a_0=3.983 Å is the lattice constant of Al) as the entire system with the innermost $4a_0 \times 4a_0 \times a_0$ as the region I. The distance that ρ^{I} extends to the region II is 2.61 Å, and the size of the periodic box is $8a_0 \times 8a_0 \times a_0$. Figure 2(a) presents the total local potential of the system, the local potential of the region I and the embedding potential. All these potentials are defined with respect to ρ^{I}. The total local potential consists of the local potential of the region I and the embedding potential. In Figs. 2(b) and 2(c), we show the charge density ρ^{I} and ρ^{II}, respectively.

First of all, all potentials vanish beyond Ω^{I} due to the constraint imposed on the total local potential. This constrain has successfully enforced ρ^{I} to be zero beyond Ω^{I} as shown in Fig. 2(b). ρ^{I} and ρ^{II} only overlap over a distance (around $0.5a_0$) where the embedding potential is nonzero. The fact

that ρ^{I} and ρ^{II} overlap is of crucial importance and it is the result of the self-consistent quantum mechanical coupling. The sum of both densities should give the correct total density of the system.

From Fig. 2, it is observed that the embedding potential is localized at the QM/MM interface and it decays to zero in the interior of the region I. The behavior of the total local potential at the interface is different from that at the interior of the region I; this is because the total local potential is defined with respect to ρ^{I} which is equal to ρ^{tot} only at the interior of the region I but not at the interface. Once the total local potential associated with ρ^{II} is included, the total local potential would be periodic throughout the entire space for the perfect lattice.

III. APPLICATIONS

In this section, we apply the QM/MM method to study the interactions between H and the extended defects in Al including the edge dislocation and GB. For the kernel term in OF-DFT, we use the Wang-Govind-Carter kinetic-energy functional with the density-dependent kernel and parameters $\{\alpha,\beta,\gamma\}=\{5/6+\sqrt{5}/6,5/6-\sqrt{5}/6,2.7\}$.[19] The Perdew-Zunger local-density approximation[25] is used to evaluate the exchange-correlation functional for Al. The projected augmentation wave method[26,27] is employed for the pseudopotential. The k points are sampled according to the Monkhorst-Pack scheme.[28] We use the so-called "force-matching" EAM potential[29,30] for the MM simulations. The EAM potential has been scaled to yield precisely the same lattice constant and bulk modulus as the corresponding KS-DFT values.

A. H in grain boundary

In this section, we employ the QM/MM method to examine H-GB interaction focusing on H binding at various sites and the H diffusion in the GB. In the $\Sigma 5\{210\}[001]$ symmetric tilt GB model (Fig. 3), the x, y, and z axis correspond to $[1\bar{2}0]$, [210], and [001], respectively, and the periodic boundary conditions are applied in the x and z directions. The model measures 17.81 Å $\times$ 185 Å $\times$ 11.95 Å with 2388 atoms in total. The dimensions of the region I are 17.81 Å $\times$ 28.40 Å $\times$ 11.95 Å with 180 DFT atoms. The GB plane is located at the center of the region I. We use a force-based conjugate gradient method to optimize the ionic structure of the entire system with the total energy given by Eq. (1). The relaxation for all ions is performed until the maximum force on any ion is less than 0.04 eV/Å. In the KS-DFT calculations, a plane-wave cutoff of 300 eV is used and the k points are sampled with a $3\times1\times3$ mesh. The NEB method has been implemented in the QM/MM approach and is used to determine the diffusion paths and the corresponding energy barriers.

First we determine the site preference of an interstitial H at the GB. We find that the energetically most favorable position for the H atom is not **H1** on the GB plane (Fig. 3) but rather at positions (referred as **H1′** in the following) slightly off the GB plane ($\pm$0.8 Å) whose energy is 0.015 eV lower.

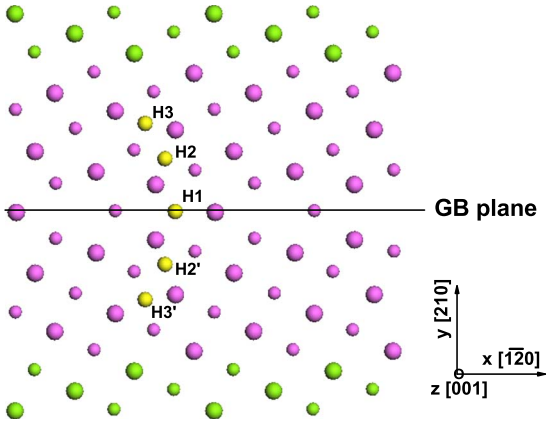

FIG. 3. (Color online) Atomic structure of $\Sigma 5\{210\}[001]$ symmetric tilt grain boundary. The smaller spheres represent the atoms that are farther away from the page in [001] axis. The magenta and green spheres represent the atoms in the region I and II (partially shown), respectively. The yellow spheres denote the interstitial H atoms.

These preferred positions correspond to the tetrahedral sites above and below the GB plane in the perfect lattice. In other words, the GB does not perturb much the preferred H bulk position. As shown in Fig. 4(b), the H impurity attracts the valence electrons from the neighboring Al atoms and becomes negatively charged; the ionic bonding between H and the Al atoms has a directional character in accordance with its local structure. To assess the energetic stability of H at the GB, we calculate H-GB binding energy $\Delta E_{\mathrm{GB}}[\mathrm{H}]$ defined as

$$\Delta E_{\mathrm{GB}}[\mathrm{H}] = E_c[\mathrm{GB}+\mathrm{H}] - E_c[\mathrm{GB}], \tag{5}$$

where $E_c[\mathrm{GB}+\mathrm{H}]$ and $E_c[\mathrm{GB}]$ are the cohesive energy of the GB with and without the interstitial H atom, respectively. We find that the binding energy $\Delta E_{\mathrm{GB}}[\mathrm{H}]$ at three representative sites **H1′**, **H2**, and **H3** is −3.00 eV, −2.82 eV, and −2.89 eV, respectively. As a comparison, we have also cal-

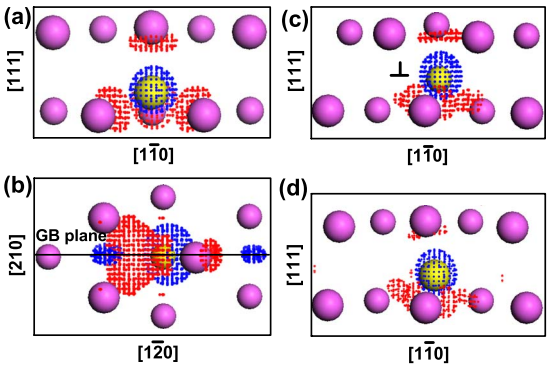

FIG. 4. (Color online) Interstitial H in (a) Bulk, (b) GB, (c) LP, and (d) SF, respectively. The blue (red) isosurfaces illustrate the bonding charge density (difference between the solid charge density and the superposition of the atomic charge densities) distribution at +(−) 0.06 Å^{-3}. The positive (negative) bonding charge density represents electron accumulation (depletion) in forming the solid. The yellow (magenta) spheres denote H (Al) atoms; the smaller spheres represent that the atoms are farther away from the page.

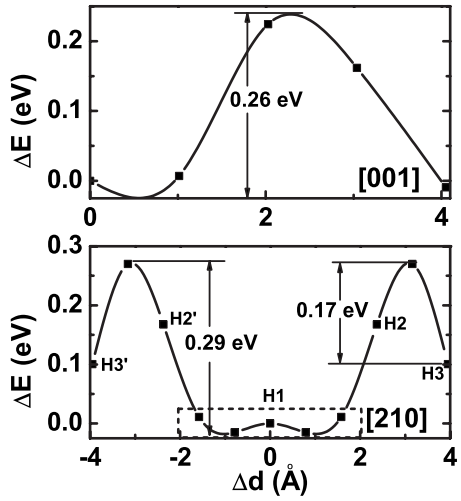

FIG. 5. Top panel: the energy profile for the interstitial H atom (**H1** in Fig. 3) diffusing along [001] direction at the GB plane. Bottom panel: the energy profile for the interstitial H atom diffusing across the GB plane. The diffusion path is **H3′**→**H1**→**H3**. Δd denotes the atomic displacement with respect to **H1**.

culated the H binding energy in bulk Al. To this end, we use the stand-alone VASP calculation since the system is much smaller than the GB. The dimensions of the supercell in the VASP calculation are 14.08 Å×13.80 Å×14.63 Å along $[1\bar{1}0]$, [111], and $[11\bar{2}]$ directions, respectively. Similar to Eq. (5), we define the H binding energy in bulk, $\Delta E_{\mathrm{Bulk}}[\mathrm{H}]$ as

$$\Delta E_{\mathrm{Bulk}}[\mathrm{H}] = E_c[\mathrm{Bulk}+\mathrm{H}] - E_c[\mathrm{Bulk}], \tag{6}$$

where $E_c[\mathrm{Bulk}+\mathrm{H}]$ and $E_c[\mathrm{Bulk}]$ are the cohesive energy of the bulk with and without the interstitial H, respectively. We have examined both tetrahedral and octahedral sites for the H interstitial; we find that the tetrahedral site is energetically more favorable than the octahedral site—the binding energy differs by 0.07 eV. The H binding energy $\Delta E_{\mathrm{Bulk}}[\mathrm{H}]$ at the tetrahedral site is −2.88 eV. Therefore the H atom prefers to occupy the interstitial site at the grain boundary over the tetrahedral site in the bulk. The H binding energy difference between the bulk and the GB is 0.12 eV, agreeing very well the experimental value of 0.15 eV.[31] The tetrahedral site in the bulk corresponds to **H3** (or **H3′**) site where the H atom forms four ionic bonds with the four-nearest-neighbor (NN) Al atoms at the tetrahedral vertices as shown in Fig. 4(a). The fact that $\Delta E_{\mathrm{GB}}[\mathrm{H3}]$ (−2.89 eV) matches very well $\Delta E_{\mathrm{Bulk}}[\mathrm{H}]$ (−2.88 eV) demonstrates that the QM/MM method can reproduce very accurately the stand-alone VASP results.

Next we study the interstitial H diffusion in the GB by considering two diffusion paths: (1) along the GB plane and (2) across the GB plane. In the first case, the interstitial H atom moves along [001]—the tilt axis of the GB. We find that diffusion energy barrier is 0.26 eV as shown in Fig. 5(a). In this case, the H atom moves in the GB plane but slightly deviates from the diffusion direction attracted by the neighboring Al atoms. For comparison purpose, we have also calculated the diffusion energy barriers of the interstitial H in bulk Al and the results are listed in Table I. The lowest diffusion energy path is from one tetrahedral site to the next tetrahedral site in the (111) plane and along $[1\bar{1}0]$ direction. The calculated bulk diffusion energy barrier is 0.17 eV. On the other hand, the corresponding energy barrier is 0.40 eV if the H atom diffuses between the neighboring tetrahedral sites along [001] direction. Therefore as far as the [001] diffusion is concerned, the $\Sigma 5\{210\}[001]$ GB could provide a faster diffusion channel or a pipe than the bulk with two orders of magnitude increase in diffusivity at 300 K. For the H diffusion across the GB plane from **H3′** to **H3**, we summarize the results in Fig. 5(b). We find that the interstitial H needs to overcome an energy barrier of 0.17 eV to reach the GB while it requires a much higher energy barrier of 0.29 eV to escape from the GB. This asymmetry is due to the strong H-GB binding which attracts the H impurities to the GB from the bulk. Although there is an energy barrier for the H diffusion from **H3** (or **H3′**) to **H2** (or **H2′**), the subsequent diffusion into the GB region is spontaneous. We also find that there is a narrow band of 4 Å in width where the interstitial H atoms prefer to segregate [dashed box in Fig. 5(b)]. This narrow band could provide trapping sites for the H impurities once they reach the GB region, consistent with experimental observations.[21]

B. H in edge dislocation

Dislocations are of crucial importance to plastic deformation in materials. In fcc metals, dislocations can reduce its elastic energy by dissociating into two Shockley partials connected by a stacking fault (SF).[32] An accurate simulation of dislocation core structure is challenging due to the following reasons: (1) in order to capture the severe deformation and possible bond breaking at the dislocation core, quantum mechanical calculations are often required; (2) standard *ab initio* quantum mechanical calculations employ either PBC or open boundary conditions (OBC). Neither is satisfactory for many cases. The PBC lead to fictitious interaction among

TABLE I. H binding energy $\Delta E[\mathrm{H}]$ (in eV), diffusion direction, and diffusion energy barriers ΔE^{m} (in eV) of H in bulk, the grain boundary and the edge dislocation (LP and SF), respectively.

		Bulk		GB	LP	SF
$\Delta E[\mathrm{H}]$		−2.88		−3.00	−3.00	−2.78
Direction	$[1\bar{1}0]$	$[11\bar{2}]$	[001]	[001]	$[11\bar{2}]$	$[11\bar{2}]$
ΔE^{m}	0.17	0.32	0.40	0.26	0.38	0.20

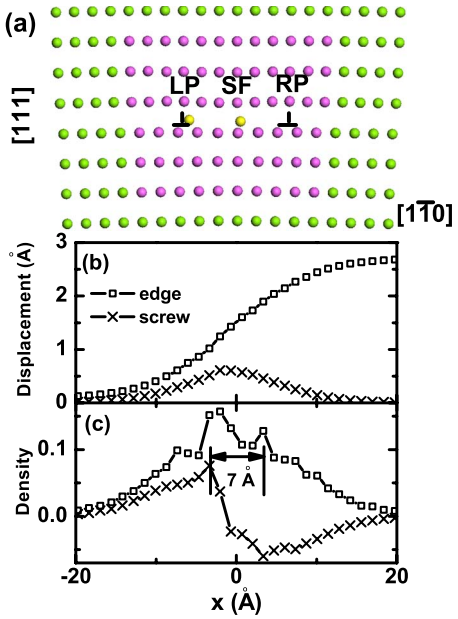

FIG. 6. (Color online) (a) Atomic structure of the edge dislocation. LP and RP represent the left and right Shockley partial, respectively, and the stacking fault ribbon is denoted as SF. The magenta and green spheres represent the atoms in the region I and II (partially shown), respectively. The yellow spheres denote the interstitial H atoms at LP and SF. The edge and screw components of the relative atomic displacement and the displacement density as a function of x are shown in (b) and (c), respectively, for pure Al. The double peak in the density plot illustrates the distance between the two partials as 7 Å.

dislocation images if the simulation cell is not large enough. If the dislocation dissociates into partials, the problem could be even worse. On the other hand, the OBC involve fictitious interaction between the dislocation and surfaces. Recently, a first-principles lattice Green's-function boundary condition method (FP-GFBC) has been proposed which appears effective to alleviate some of the problems mentioned above.[33] In this section, we first employ the QM/MM method to simulate the core structure of the edge dislocation in Al with comparisons to other experimental and theoretical results. Then we study the interaction between the H impurity and the dislocation by examining the site preference and the H diffusion along the dislocation line.

In the computational model shown schematically in Fig. 6(a), the x, y, and z axis correspond to $[1\bar{1}0]$, [111], and $[11\bar{2}]$, respectively, and the PBC is applied in the z direction (along the dislocation line). The entire system consists of 169 Å $\times$ 69 Å $\times$ 14.634 Å with 10 710 atoms in total. The dimensions of the region I are 14.42 Å $\times$ 11.50 Å $\times$ 14.634 Å with 198 KS-DFT atoms and the rest of the system belongs to the region II, including 10512 EAM atoms. The core of the $a/2\langle 110\rangle$ edge dislocation is located at the center of the region I. The repeating distance along the z axis is *three times* of the minimal periodicity along the z direction which is crucially important for describing H diffusion. The H impurities are separated by ~15 Å along the dislocation line so that the fictitious interaction between the periodic images of H is largely removed. The computational parameters are similar to the grain boundary calculations but with the k points sampled in a $1\times1\times3$ mesh.

The dislocation core structure of pure Al is presented in Fig. 6. Here we use the relative atomic displacement across the dislocation slip plane along the x and z directions to represent the edge and screw components of the strain field, respectively. The derivative of the relative displacement with respect to x gives the corresponding dislocation density. The double peak in the dislocation density plot suggests that the dislocation is dissociated into two Shockley partials whose positions are represented by the peaks. Accordingly, we find the partial separation distance as 7 Å. For comparisons, experimental measurement from the weak-beam transmission electron microscopy reports a value of 8.0 Å for the separation distance in Al.[34] The theoretical value determined by the FP-GFBC method ranges from 7.0 to 9.5 Å.[33] A multiscale QCDFT method gives a value of 5.6 Å.[35] A QM/MM mechanical coupling approach yields a value of 5.6 Å as well.[36] The MM simulations based on empirical potentials have reported a rather scattered results ranging from 5.4–6.2 Å,[37] to 14.7 Å (Ref. 33) and 16.0 Å.[38] Since the displacement field is defined on a discrete lattice of atoms which are separated by the NN distance of 1.4 Å in the x direction, there is an intrinsic uncertainty in determining the dislocation position. This uncertainty is in the same order (~1.4 Å) of the NN distance. In light of this uncertainty, the present QM/MM result compares very well with the experimental value. Finally, because each theoretical method determines the separation distance differently, the actual discrepancies may not be as alarming as they appear to be.

Next, we determine the site preference of the interstitial H at the dislocation core. Two sites are considered: one is at the core of a partial dislocation, and the other is at the SF ribbon. Since the two Shockley partials are equivalent, we focus on the left partial (LP) only. As shown in Figs. 4(c) and 4(d), the interstitial H atom prefers to stay on the slip plane, and forms ionic bonding with the neighboring Al atoms. Similar to Eq. (5), we can define the H binding energy with the dislocation, $\Delta E_{\mathrm{LP(SF)}}[\mathrm{H}]$ as

$$\Delta E_{\mathrm{LP(SF)}}[\mathrm{H}] = E_c[\mathrm{LP(SF)} + \mathrm{H}] - E_c[\mathrm{Disl}], \tag{7}$$

where $E_c[\mathrm{LP(SF)+H}]$ is the cohesive energy of the dislocation with an interstitial H atom in LP (SF), and $E_c[\mathrm{Disl}]$ is the cohesive energy of the dislocation. As shown in Table I, we find that $\Delta E_{\mathrm{LP}}[\mathrm{H}] < \Delta E_{\mathrm{Bulk}}[\mathrm{H}] < \Delta E_{\mathrm{SF}}[\mathrm{H}]$. Therefore the H binds most strongly with the partial core and least strongly with the stacking fault. On the other hand, the H binding energy difference between the bulk and the LP is 0.12 eV, which is the same with a previous theoretical result.[39]

Figure 7 summarizes the results of the interstitial H diffusion along LP and SF. For H diffusion along LP, there is only one energy barrier of 0.38 eV. In contrast, there are two energy barriers for the H diffusion along SF with the largest one of 0.20 eV. In other words, the H atom could be trapped between the two barriers. Relative to the bulk diffusion barrier of 0.32 eV along the $[11\bar{2}]$ direction, the stacking fault ribbon provides a faster pathway or a pipe for H diffusion with two orders of magnitude increase in diffusivity at 300

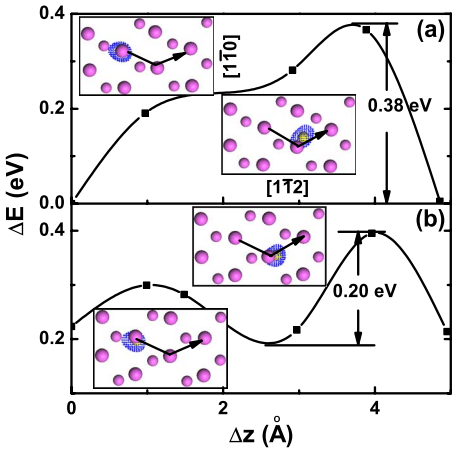

FIG. 7. (Color online) The energy profile for the interstitial H diffusion along (a) LP and (b) SF, respectively. Inset: the schematic trajectory of the H atom along the diffusion path on the (111) plane. The arrow indicates the diffusion direction. The magenta and yellow spheres represent Al and H atoms, respectively. The blue isosurfaces illustrate the charge density distribution at 0.27 $Å^{-3}$. The smaller spheres represent the atoms that are farther away from the page in [111] axis.

K. On the other hand, the partial dislocation core is not a pipe. It is interesting to contrast the present results to that of Si diffusion in the same dislocation.[22] Because Si atom has a much larger radius than H atom, it occupies the substitutional site in Al. As a result, the bulk diffusion of a Si impurity involves the formation of a vacancy, hence a much higher energy barrier (1.26 eV). On the other hand, the interstitial H impurity can diffuse in the absence of vacancies. Therefore although both SF and LP can act as pipes for Si, only SF can accelerate the H diffusion. Moreover, Si moves by "pushing its way through" with Al-Si covalent bonds being compressed—the neighboring Al atoms are significantly distorted during the diffusion. In contrast, H is attracted to the nearest neighbor Al atoms and tightly bonded with them. There is very little disturbance to the Al lattice during the H diffusion and the ionic Al-H bonding remains intact. Finally, it appears that SF provides a faster diffusion pipe for both Si and H, regardless of their different atomic sizes, bonding characters and occupation sites.

IV. CONCLUSION AND OUTLOOK

We have presented a self-consistent embedding QM/MM method that is based on the plane-wave pseudopotential KS-DFT formalism for treating the QM region. The implementation of the method, including the construction of the Hamiltonian and the behavior of the embedding potential is discussed. The QM/MM method is applied to study the interaction of H impurities with the extend defects in Al. We find that H binds strongly to both the GB and the dislocation. It is energetically most favorable for H to be at either the GB (close to the GB plane) or at the partial dislocation core; it is less favorable for H at the bulk tetrahedral site and least favorable at the stacking fault. Both the GB and the stacking fault ribbon are found to provide a faster diffusion channel along the relevant directions as compared to the bulk diffusion. There exist trapping sites for the H atoms in the GB region and along the stacking fault ribbon resulting from the energy barriers bracketing these sites. Finally, the stacking fault ribbon turns out to be a faster diffusion pipe than the partial core for both the interstitial and substitution impurities in Al.

In terms of future development of the QM/MM method, we expect a continued improvement of the kinetic-energy functional[40,41] which is used in the interaction energy calculation. Such an improvement is crucial for the method to handle a broad class of materials. Another important development has to do with magnetism which involves two components of the spin density in MM region and the spin-polarized DFT calculations in QM region. The implementation and application of the QM/MM method for molecular dynamics are underway. Finally, the same embedding approach can be generalized to study molecular plasmonics. In this case, a time-dependent DFT is coupled to quantum hydrodynamic models, which can address electronic dynamics at a larger length scale.

ACKNOWLEDGMENTS

This work was supported in part by NSF under Grant No. DMR-0611562 and DOE under Grant No. DE-FC02-06ER25791. The computational facility was supported by NSF under Grant No. DMR-0958596.

[1] G. Lu and E. Kaxiras, in *Handbook of Theoretical and Computational Nanotechnology*, edited by M. Rieth and W. Schommers (American Scientific, Stevenson Ranch, CA, 2004), Chap. 22.
[2] N. Bernstein, J. R. Kermode, and G. Csanyi, Rep. Prog. Phys. **72**, 026501 (2009).
[3] H. Lin and D. G. Truhlar, Theor. Chem. Acc. **117**, 185 (2007).
[4] I. Antes and W. Thiel, ACS Symp. Ser. **712**, 50 (1998).
[5] J. Gao and D. G. Truhlar, Annu. Rev. Phys. Chem. **53**, 467 (2002).
[6] T. A. Wesolowski and A. Warshel, J. Phys. Chem. **97**, 8050 (1993).
[7] N. Govind, Y. A. Wang, A. J. R. da Silva, and E. A. Carter, Chem. Phys. Lett. **295**, 129 (1998).
[8] T. Klüner, N. Govind, Y. A. Wang, and E. A. Carter, Phys. Rev. Lett. **86**, 5954 (2001).
[9] N. Choly, G. Lu, W. E, and E. Kaxiras, Phys. Rev. B **71**, 094101 (2005).
[10] X. Zhang and G. Lu, Phys. Rev. B **76**, 245111 (2007).
[11] X. Zhang, C. Y. Wang, and G. Lu, Phys. Rev. B **78**, 235119 (2008).
[12] P. Cortona, Phys. Rev. B **44**, 8454 (1991).
[13] M. Hodak, W. Lu, and J. Bernholc, J. Chem. Phys. **128**, 014101

(2008).
[14] G. Kresse and J. Hafner, Phys. Rev. B **47**, 558 (1993); **49**, 14251 (1994).
[15] G. Kresse and J. Furthmuller, Phys. Rev. B **54**, 11169 (1996).
[16] G. Kresse and J. Furthmuller, Comput. Mater. Sci. **6**, 15 (1996).
[17] G. Henkelman, B. P. Uberuaga, and H. Jonsson, J. Chem. Phys. **113**, 9901 (2000).
[18] L. W. Wang and M. P. Teter, Phys. Rev. B **45**, 13196 (1992).
[19] Y. A. Wang, N. Govind, and E. A. Carter, Phys. Rev. B **60**, 16350 (1999).
[20] P. García-González, J. E. Alvarellos, and E. Chacon, Phys. Rev. B **53**, 9509 (1996).
[21] S. M. Myers, M. I. Baskes, H. K. Birnbaum, J. W. Corbett, G. G. Deleo, S. K. Estreicher, E. E. Haller, P. Jena, N. M. Johnson, R. Kirchheim, S. J. Pearton, and M. J. Stavola, Rev. Mod. Phys. **64**, 559 (1992).
[22] X. Zhang and G. Lu, Phys. Rev. B **82**, 012101 (2010).
[23] M. S. Daw and M. I. Baskes, Phys. Rev. B **29**, 6443 (1984).
[24] R. M. Martin, *Electronic Structure: Basic Theory and Practical Methods* (Cambridge University Press, Cambridge, 2004).
[25] J. P. Perdew and A. Zunger, Phys. Rev. B **23**, 5048 (1981).
[26] P. E. Blöchl, Phys. Rev. B **50**, 17953 (1994).
[27] G. Kresse and D. Joubert, Phys. Rev. B **59**, 1758 (1999).
[28] H. J. Monkhorst and J. D. Pack, Phys. Rev. B **13**, 5188 (1976).
[29] F. Ercolessi, M. Parrinello, and E. Tosatti, Philos. Mag. A **58**, 213 (1988).
[30] F. Ercolessi and J. Adams, Europhys. Lett. **26**, 583 (1994).
[31] R. A. H. Edwards and W. Eichenauer, Scr. Metall. **14**, 971 (1980).
[32] J. P. Hirth and J. Lothe, *Theory of Dislocations*, 2nd ed. (Wiley, New York, 1982).
[33] C. Woodward, D. R. Trinkle, L. G. Hector, and D. L. Olmsted, Phys. Rev. Lett. **100**, 045507 (2008).
[34] W. Höllerbauer and H. P. Karnthaler, Beitrage zur elektronenmikroskopischen Direktabbildung vor Oberflachen **14**, 361 (1981).
[35] G. Lu, E. B. Tadmor, and E. Kaxiras, Phys. Rev. B **73**, 024108 (2006).
[36] Y. Liu, G. Lu, Z. Chen, and N. Kioussis, Modell. Simul. Mater. Sci. Eng. **15**, 275 (2007).
[37] Y. Mishin, D. Farkas, M. J. Mehl, and D. A. Papaconstantopoulos, Phys. Rev. B **59**, 3393 (1999).
[38] S. G. Srinivasan, X. Z. Liao, M. I. Baskes, R. J. McCabe, Y. H. Zhao, and Y. T. Zhu, Phys. Rev. Lett. **94**, 125502 (2005).
[39] G. Lu, Q. Zhang, N. Kioussis, and E. Kaxiras, Phys. Rev. Lett. **87**, 095501 (2001).
[40] J. Chai, V. L. Ligneres, G. Ho, E. A. Carter, and J. D. Weeks, Chem. Phys. Lett. **473**, 263 (2009).
[41] C. Huang and E. A. Carter, Phys. Rev. B **81**, 045206 (2010).